ARTICLE OPEN

Check for updates

Fundamental insights into the stabilisation and chemical degradation of the corrosion product scales

Xiaoqi Yue[1,2], Lei Zhang[1,3] and Yong Hua [ID][4 ✉]

Carbonate stability plays a crucial role in clarifying the evolution and protection of the naturally formed corrosion scales on the steel surface in the application of geothermal production. In this paper, the stability of the corrosion scales from both micro and atomic level are studied via a combination of electrochemistry, surface analysis and first-principle calculation. The chemical and physical characterisation of various iron–calcium mixed carbonates are experimentally analysed and results are compared with the first-principle calculation. In the presence of Ca^{2+}, the preferential loss of Ca during the dissolution experiments was observed, the interactions within the crystal weaken where Ca^{2+} co-precipitation, confirmed by a faster degradation rate for $Ca_{0.51}Fe_{0.49}CO_3$ than $FeCO_3$. This work reveals the degradation and protection performance of the naturally formed carbonate layers and provides insights into understanding the corrosion product stability and chemical breakdown of the corrosion scales.

INTRODUCTION

Ensuring engineering integrity while reducing the cost is the eternal topic for all industries such as oil and gas, geothermal, and nuclear. The research and development of corrosion-resistant alloys (CRAs) can achieve the material integrity aspect while the rise in cost restricted the applications[1]. Carbon steel was widely used in the industry such as oil and gas or geothermal productions based on its low cost and excellent mechanical performance[2–6]. However, carbon steel was subject to corrosion in the presence of CO_2, resulting in the fast iron dissolution, and followed by the development of the corrosion products gradually covering the surface and effectively reduce the corrosion behaviour[2,7,8].

Iron carbonate ($FeCO_3$), for example, formed on the surface was considered as a natural protective scale to prolong the lifetime of carbon steel[2,7,9,10]. A large amount of previous research has adverted the $FeCO_3$ protection to the surface through forming $FeCO_3$ scales under amorphous or crystalline state[6,11,12]. The coverage and compactness for the development of $FeCO_3$ scales were fully discussed in the literature in terms of crystal sizes[13–15], orientation[16], solution pH[12,17], and other factors[12,18].

Recent studies found that simplified corrosion products such as $FeCO_3$ can misestimate the corrosion product protection to the steel[19–22]. Esmaeely et al.[20] revealed that the presence of high concentration Ca^{2+} to be responsible for the growth of $Ca_{1-x}Fe_xCO_3$ on the surface. Similar work done by Hua et al.[21] indicated that the associated effects of Cl^-, Ca^{2+}, Mg^{2+}, and CO_2 within brine solution on the growth of the corrosion scales, they reported that the presence of Ca^{2+} prefers to co-precipitation within the crystalline $FeCO_3$ and accentuates the total penetration rate of carbon steel. Shamsa et al.[22] verified the addition of Ca^{2+} led to the growth of a less protective $Ca_{1-x}Fe_xCO_3$ scale which not only accelerated the pit growth but also increased the general corrosion rate.

The structures for various carbonates $FeCO_3$(siderite), $MgCO_3$ (magnesite) and $CaCO_3$ (calcite) have been studied for decades since they are extensively present in Earth's crust[23]. Faruque et al.[24] reported the electronic and bonding properties of rhombohedral $CaCO_3$ and found the indirect energy gap to be 5.07 eV. Brik[25] revealed that the calcite conduction band is much narrower than the one of magnesite. Elizabeth et al.[26] investigated the dolomite ($CaMg(CO_3)_2$) (1 0 4) phase and showed the Mg and Ca atoms have different bond distances with oxygen atoms and the main Ca–O interatomic distances turned to be greater after optimization of the surface. The analysis from Golosova et al.[27] demonstrated that the anisotropic lattice compression of siderite was mainly contributed by the Fe–O bonds. Han et al.[28] calculated the interactions of iron in $Mg_{1-x}Fe_xCO_3$ from the iron-poor ($x = 0.125$) to the iron-rich ($x = 1$, $FeCO_3$ siderite) and found that the volume difference concerning $MgCO_3$ changes with Fe doping and resulted in the difference in relative enthalpy. Numerous studies reported that the effects of pressure, temperature, and metal ion doping concerning structure optimization and electron distribution for carbonates. However, rare results regarded the mixture carbonates as corrosion products and focused on their corrosion protection to the surface as well as their electron distribution changes during the corrosion reactions.

To reveal the protectiveness of the corrosion scales, samples covered by $FeCO_3$ layers, iron-calcium carbonate layers, and calcium-containing corrosion product layers were prepared by high temperature and high-pressure corrosion tests. The dissolution of these complex compounds was established through exposed them to a CO_2-saturated solution at and pH of 3.75. Linear polarisation resistance (LPR) and electrochemical impedance spectroscopy (EIS) methods were used for tracking the degradation of the corrosion scales. In addition, first-principle thermodynamics based on the density functional theory (DFT) were used to provide a detailed theoretical investigation on the required calcium effects of bond energy, atomistic and electronic structure of the crystals, and was associated with the corrosion product protection to the surface. It is crucial to study these effects on the true protective performance of the corrosion products and reveal the stability of the naturally formed corrosion

[1]Institute of Advanced Materials and Technology, University of Science and Technology Beijing, Beijing, China. [2]Shunde Graduate School, University of Science and Technology Beijing, Foshan, China. [3]Beijing Advanced Innovation Center for Materials Genome Engineering, University of Science and Technology Beijing, Beijing, China. [4]Institute of Functional Surfaces School of Mechanical Engineering, University of Leeds, Leeds, UK. ✉email: Y.Hua@leeds.ac.uk
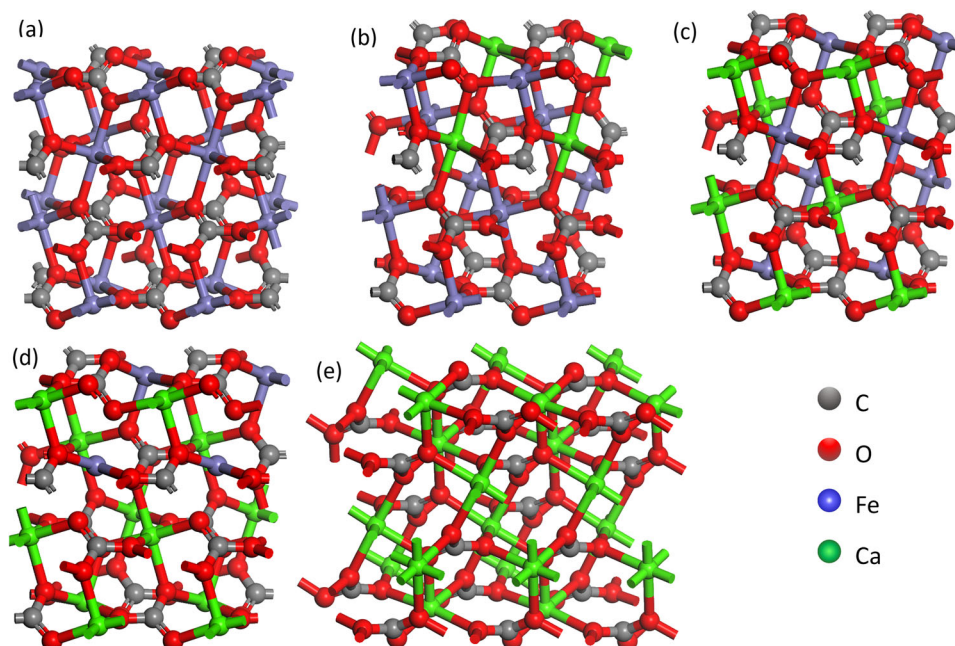
Fig. 1 Various crystal structures for $Ca_{1-x}Fe_xCO_3$. a $FeCO_3$ siderite, **b** $Ca_{0.25}Fe_{0.75}CO_3$, **c** $Ca_{0.5}Fe_{0.5}CO_3$, **d** $Ca_{0.75}Fe_{0.25}CO_3$, and **e** calcite.
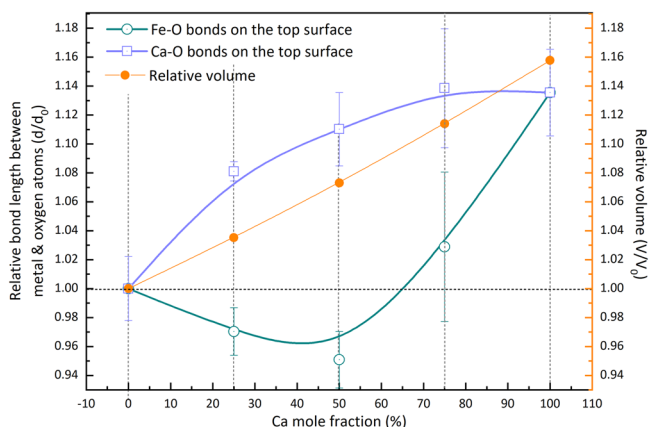

Fig. 2 The calculation of the nearest Fe–O and Ca–O bonds on the top surface. The length calculations of Fe–O (purple) bonds and Ca–O (green) bonds at various Ca mole fraction on the top surface.

scales to be effective in corrosion protection for carbon steel under geothermal applications.

RESULTS

Stability properties of corrosion products caused by Ca doping

Supercells of $Ca_{1-x}Fe_xCO_3$ doping with various Ca mole fractions were calculated and compared with pure siderite ($FeCO_3$, $x = 1$) and pure calcite ($CaCO_3$, $x = 0$), with the preferred orientation along the plane (1 0 4), as shown in Fig. 1a–e. The results summarised in Fig. 2 represent the characteristics of various $Ca_{1-x}Fe_xCO_3$, Ca mole fraction contains from Ca-poor ($x = 0$) to Ca-rich ($x = 1$) and found the average Fe–O distance for $FeCO_3$ is 2.1 Å, while the average bond length between Ca and O turns to be 2.4 Å for $CaCO_3$ at the top surface. The replaced sites by Ca results in the weakening of interaction between Ca cations and C–O_3 for $Ca_{1-x}Fe_xCO_3$ ($x > 0$), the length for Ca–O bonds in $Ca_{0.25}Fe_{0.75}CO_3$ and $Ca_{0.5}Fe_{0.5}CO_3$ increased by compressing the bond length of Fe–O, which suggests the non-uniform bond energy within $Ca_{1-x}Fe_xCO_3$. As the

co-precipitation of Ca^{2+} approached 75%, the increase in the bond length of Ca–O dominated the lattice parameter and resulting in the total volume expansion and leading to the increase in the bond length of Fe–O as well, which suggests that the stability for both Ca–O and Fe–O bonds decreased for $Ca_{1-x}Fe_xCO_3$ compared with pure $FeCO_3$.

Since Fe atoms were replaced by Ca atoms within the crystal, the unit-cell volume of $Ca_{1-x}Fe_xCO_3$ expends to a looser arrangement than $FeCO_3$, and the unit-cell approaches the volume of $CaCO_3$ as the increase in the mole fraction of Ca within the unit-cell.

The electron density for $FeCO_3$ and $Ca_{1-x}Fe_xCO_3$ structures are provided to visualize the effect of Ca^{2+} co-precipitation. It can be seen that C and O atoms join via high electron density and form a molecular structural unit connected by strong covalent bonds for $FeCO_3$. In the regions around Fe ions in Fig. 3a, there are electrons overlaps to the adjacent oxygen, indicating the covalent contribution is seen between Fe and O atoms with the predominant of the ionic bond[27,29].

After the co-precipitation of Ca^{2+} as shown in Fig. 3b, no electron interaction is observed between Ca and O considering the relatively longer distance than that of Fe–O. However, the constraint bond exists between Fe and O atoms and enhances with the increase of Ca^{2+} co-precipitation level from 25 to 50%, accompanied by the rotation of the plane of C–O_3 molecular structural units due to the repulsion of the calcium atoms (Fig. 3c). When the Ca contents approach 75%, the expanded volume resulted in a decrease in the interactions between cations and oxygen, such as Ca–O and Fe–O bonds (Fig. 3d). The difference of electron density between Ca–O bonds and Fe–O bonds suggests the preferential for Ca–O bonds break during the dissolution of iron–calcium mixed carbonate into ions.

Many studies have proved the growth of the carbonated corrosion scales by the precipitation/dissolution processes[10,30–32]. The steel substrate beneath the carbonates suffered localised corrosion since the naturally formed corrosion scales are porous and local dissolution of the corrosion scales can occur at the material interface. Figure 4 provides examples of $Ca_{0.5}Fe_{0.5}CO_3$ dissolution by losing Ca^{2+} and Fe^{2+}, respectively, which yields the

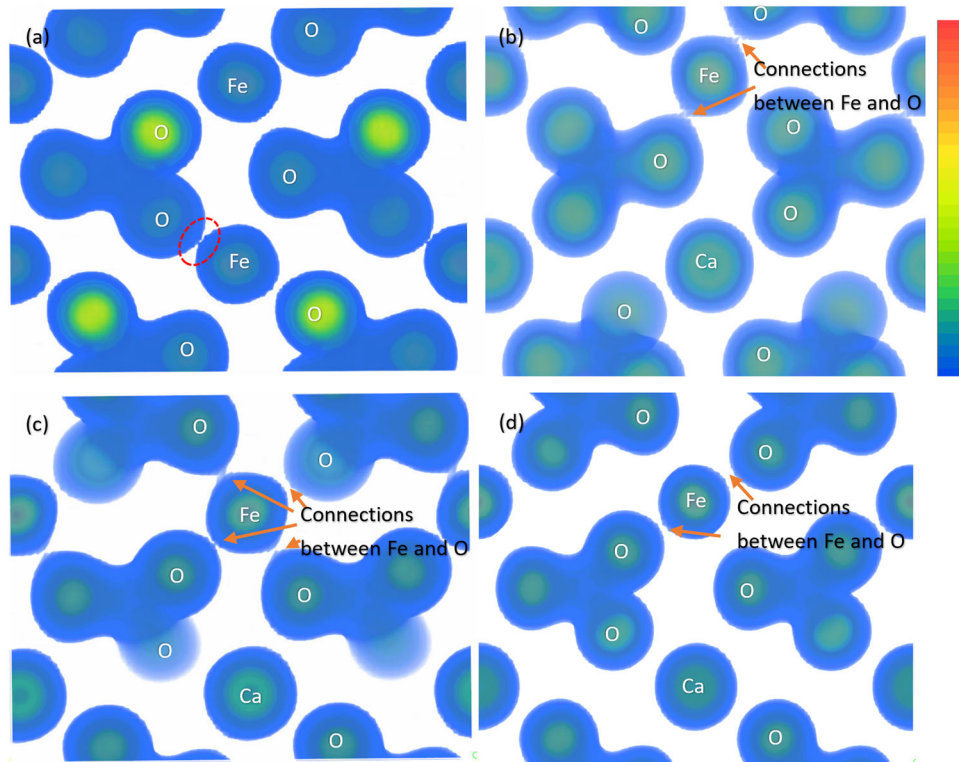**Fig. 3 Electron density of $Ca_{1-x}Fe_xCO_3$ on the top surface. a** $FeCO_3$ siderite, **b** $Ca_{0.25}Fe_{0.75}CO_3$, **c** $Ca_{0.5}Fe_{0.5}CO_3$, and **d** $Ca_{0.75}Fe_{0.25}CO_3$. The calculation of electron density of various $Ca_{1-x}Fe_xCO_3$ units on the top surface.
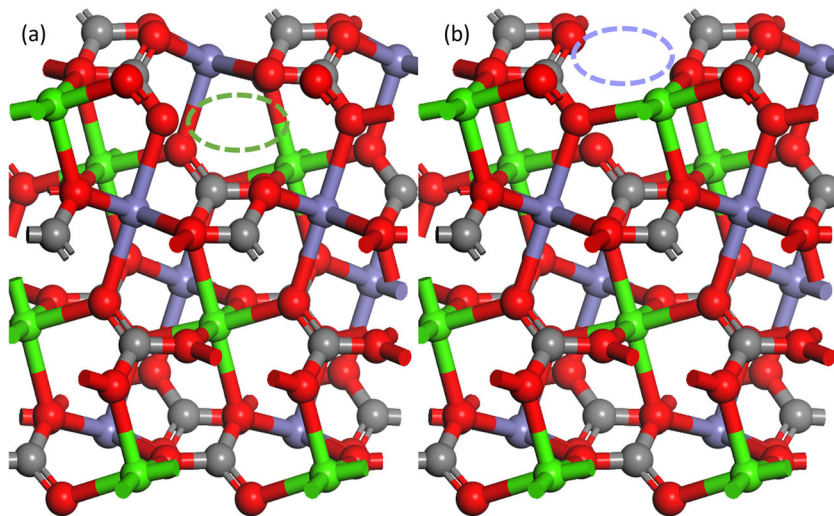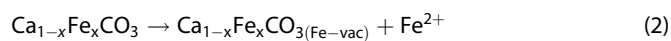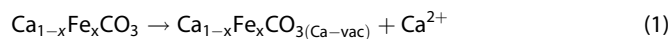

Fig. 4 Two typical ways of $Ca_{0.5}Fe_{0.5}CO_3$ dissolution. a losing Ca and **b** losing Fe. The two typical ways of $Ca_{0.5}Fe_{0.5}CO_3$ dissolution.

dissolution pathway as follows:

$$Ca_{1-x}Fe_xCO_3 \rightarrow Ca_{1-x}Fe_xCO_{3(Ca-vac)} + Ca^{2+} \tag{1}$$

$$Ca_{1-x}Fe_xCO_3 \rightarrow Ca_{1-x}Fe_xCO_{3(Fe-vac)} + Fe^{2+} \tag{2}$$

where $Ca_{1-x}Fe_xCO_{3(Ca-vac)}$ and $Ca_{1-x}Fe_xCO_{3(Fe-vac)}$ are shown as Fig. 4a, b, and the dissolution energy is expressed as follows:

$$E_{dissolution} = E_{Ca_{1-x}Fe_xCO_{3(X-vac)}} + E_{ions} - E_{Ca_{1-x}Fe_xCO_3} \tag{3}$$

The change in energy of dissolution by losing Ca^{2+} ion (785.5 kcal/mol) is smaller compared with that by losing Fe^{2+} ion (832.0 kcal/mol), suggesting the degradation of corrosion products by preferential breaking Ca–O bonds.

Effect of time on the dissolution of corrosion product scales

Once the presence of Ca^{2+} ions was found in the fluids of geological formation, the precipitation of calcium-enriched carbonates was proposed to influence the morphology and structure, as well as affecting corrosion protection to the steel surface compared with the naturally formed $FeCO_3$. To confirm the DFT calculation described above, revealing the degradation mechanisms of pure $FeCO_3$ and iron-calcium mixed carbonates, carbon steel covered by various corrosion products were prepared

in a simulated geothermal environment with/without the presence of Ca^{2+}.

Figure 5 shows the SEM images and XRD patterns of the prepared corrosion products formed in 60 °C conditions with/without the addition of Ca salts, and Supplementary Figs 3b and 4 illustrate the thickness of the corrosion scales prior to dissolution experiments. The presence of Ca^{2+} in the solution resulted in the peaks for naturally formed corrosion products shift to the left from $FeCO_3$ (purple dash lines) and toward a mixture of Fe–Ca carbonates (green dash lines), which consistent with our previous studies[21,22]. The shifted peaks from XRD measurement correspond with the increase of d-spacing for the plane (1 0 4) for iron-calcium mixed carbonate according to Bragg's law as shown in Eq. (4):

$$d = \frac{n\lambda}{2\sin\theta} \tag{4}$$

where n is a positive integer and λ is the wavelength of the incident X-ray wave. The mole fraction of calcium in the iron-calcium mixed carbonate was 0.51 according to the relationship between d-spacing and calcium proportion, the calculations are shown in Supplementary Eq. (7).

Polarisation resistance (R_p) can reflect the dissolution speed of the corrosion scales with time. The obtained in situ R_p measurements by the LPR technique are plotted in Fig. 6. The recorded R_p during the corrosion scale dissolution were determined from the slope of the line:

$$R_p = \frac{\Delta E}{\Delta I} \tag{5}$$

Purple and green symbols represent R_p for carbon steels covered by pure $FeCO_3$ and $Ca_{0.51}Fe_{0.49}CO_3$ scales exposed to the CO_2-saturated 3 wt.% NaCl solution at 15 °C respectively. For both $FeCO_3$ and $Ca_{0.51}Fe_{0.49}CO_3$ scales covered samples, high R_p values were measured at the beginning. The initial R_p for naturally formed $FeCO_3$ was higher than that of $Ca_{0.51}Fe_{0.49}CO_3$, suggesting that the sample covered with $FeCO_3$ has a lower initial corrosion rate. For stage 2, a sharp R_p reduction was recorded for the sample covered with $Ca_{0.51}Fe_{0.49}CO_3$ due to the scale dissolved fast with immersion time in comparison with the sample covered with $FeCO_3$. A relatively stable R_p was recorded at stage 3 after 1000 min for the sample covered by $Ca_{0.51}Fe_{0.49}CO_3$ and similar values were measured after 6000 mins for sample surface covering $FeCO_3$, suggesting the dissolution of the corrosion scales consisted of $Ca_{0.51}Fe_{0.49}CO_3$ was easier compared with pure $FeCO_3$ under the same experimental conditions.

Figure 7 presents the EIS measurements of samples exposed to the solution at each dissolution stage. The impedance measured in stage 1 suggests that the coverage of pure $FeCO_3$ on the entire surface acting as a diffusion barrier and protecting to the surface, while the $Ca_{0.51}Fe_{0.49}CO_3$ scales present a porous feature (fitting as Warburg impedance, Z_W). The aggressive ions penetrate easily through this porous layer, resulting in the fast converting to activation dissolution in stage 1.

Stage 2 corresponded to a rapid decline in R_p over the exposure time, indicating the corrosion product dissolution occurred on the surface[33]. In Fig. 7b, the Nyquist plots for $FeCO_3$-covering samples shown in stage 2 present the diffusion-controlled feature at low frequencies, revealing the generation of gaps between $FeCO_3$ crystals through the dissolution processes, which as expected that the protection for naturally formed scales is dependent on the localised corrosion scale dissolution. However, the diffusion control disappeared on Nyquist plots for $Ca_{0.51}Fe_{0.49}CO_3$-covering samples, replacing with the measured inductance arcs and suggesting the large decrease in R_p through dissolving the corrosion scales[34], accelerating the penetration where the adsorption and desorption of dissolved cations occur constantly.

For stage 3, the measured semi-circles for both $FeCO_3$ and $Ca_{0.51}Fe_{0.49}CO_3$-covering samples became smaller, suggesting that

the corrosion rates increased due to the corrosion scales dissolved from the surface. A similar observation was seen from the XRD in Supplementary Fig. 2, the most intense Bragg reflection (1 0 4) Miller planes for $Ca_{0.51}Fe_{0.49}CO_3$ showed a decrease in intensity. It is interesting to note that there is no significant difference in the intensity for $FeCO_3$-covering sample, and the measured semi-circle of the $FeCO_3$-covering sample was larger than that of $Ca_{0.51}Fe_{0.49}CO_3$-covering samples, suggesting that the crystalline $FeCO_3$ dissolved slower than $Ca_{0.51}Fe_{0.49}CO_3$. The co-precipitation of Ca^{2+} ions into the crystalline carbonate has weakened the bonds between Ca^{2+} and CO_3^{2-} and favoured the Ca–O bonds break compared to $FeCO_3$ during the dissolution, which is in agreement with DFT calculations as shown in Fig. 2.

Characterisation of the corrosion product morphology during the dissolution experiment

Figure 8 shows the morphology of corrosion scales before and after the dissolution experiments. Figure 8a represents the dense and uniform cubic $FeCO_3$ crystals and compared with the relative complex structures of $Ca_{0.51}Fe_{0.49}CO_3$ (Fig. 8c) crystals formed on the surface with the presence of 1000 ppm Ca^{2+} ions in the solution. The co-precipitation of Ca^{2+} ions into crystalline transforms the cubic morphology into globular structure crystals. Some pores were observed between these globular crystals, consistent with the impedance measured in stage 1 during the dissolution process, smaller semicircle and higher corrosion rate were obtained compared to that of sample covered with $FeCO_3$ as shown in Fig. 7.

Figures 8b and d represent the dissolved corrosion products after 120 hrs which correspond to stage 3 in Figs 6 and 7. The morphology in Fig. 8b indicates that the gaps appeared and are revealed as a result of the preferential dissolution occurring at the boundaries between $FeCO_3$ crystals. For the dissolution experiment of $Ca_{0.51}Fe_{0.49}CO_3$, the surface as shown in Fig. 8d illustrates porous corrosion products. The high magnification SEM images show the crystals were partially dissolved on the surface and resulted in porous characteristics and poor protection which agree with the EIS measurements as shown in Fig. 7d and f.

Supplementary Fig. 3 indicates the detected elemental compounds of $Ca_{0.51}Fe_{0.49}CO_3$ scales before and after dissolution by using EDS. The EDS results indicate that the proportion of Ca within the corrosion products was about 48.7% before the dissolution, this value decreased to 3.5% after dissolution experiments. The results are supported by DFT calculation which suggests the weak bonds between Ca^{2+} and CO_3^{2-} and the degradation of $Ca_{0.51}Fe_{0.49}CO_3$ by preferential breaking Ca-O bonds. It is interesting to note that the presence of Ca-rich areas was detected locally and mainly found in the pores after 120 h of dissolution (Supplementary Fig. 3e), suggesting that the growth of $Fe_xCa_{1-x}CO_3$ scales contains ununiform Ca mole fraction and results in the preferential dissolution occurred locally on the surface.

DISCUSSION

The present study helps fill the current knowledge gaps that the degradation processes of naturally formed corrosion scales occur from the micro-level to the molecular level on the surface. Combining the first-principle DFT calculations and experimental validation is an effective way that can be used to elucidate the dissolution of corrosion product scales and protection performance to the steel surface. $Ca_{0.51}Fe_{0.49}CO_3$ with a complex structure that considers the preferential orientation, composition, and interactions that yield insights into the molecular mechanisms of sensitive sites for degradation. The results of our first-principle calculations reveal that the degradation of $Ca_{0.51}Fe_{0.49}CO_3$ by preferential breaking Ca-O bonds and the required breaking
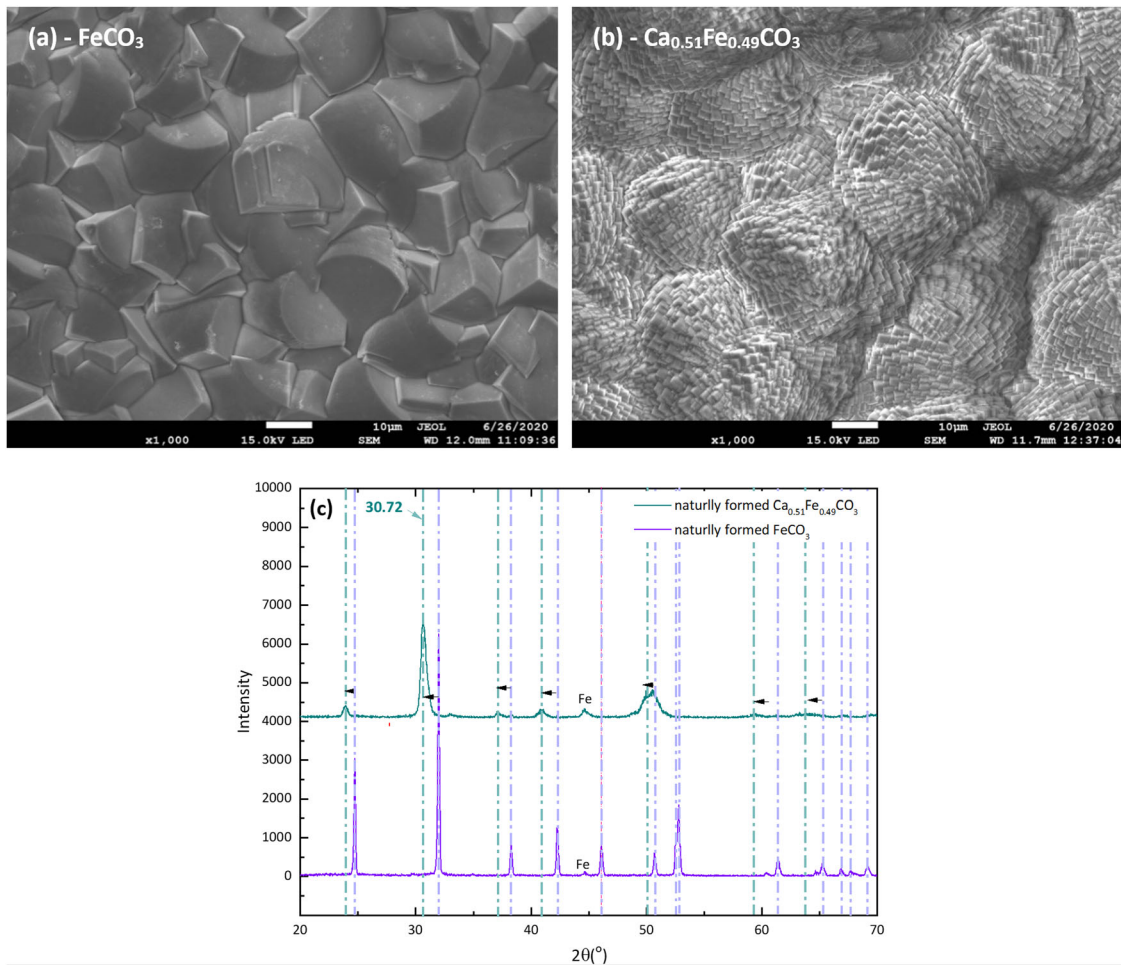
Fig. 5 Surface morphology and composition of the corrosion products. The formation of the corrosion products in 60 °C conditions with/without the addition of Ca. **a** SEM-$FeCO_3$, **b** SEM-$Ca_{0.51}Fe_{0.49}CO_3$, and **c** XRD patterns.
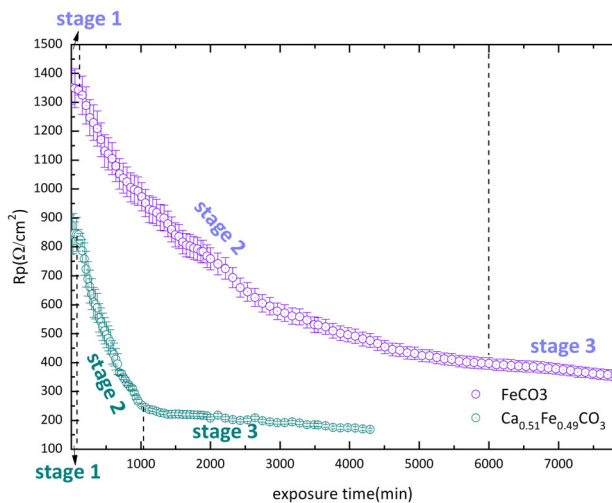

Fig. 6 In situ R_p measurements. Dissolution measurements of carbon steel covered with (purple) $FeCO_3$ or (green) $Ca_{0.51}Fe_{0.49}CO_3$ scale over time in a CO_2-saturated 3 wt.% NaCl solution at 15 °C.

energy to lose Ca is smaller than Fe in $FeCO_3$ structure (Fig. 4). The propensity of Ca dissolution within the Fe–Ca mixed carbonates accelerates with the increase of Ca^{2+} co-precipitation (Supplementary Fig. 5) and the obtained results are validated with

experimental measurements. In the absence of Ca^{2+}, the results suggest that the preferential dissolution occurs at the grain boundary, indicating the weak sites for a protective $FeCO_3$ layer. During the dissolution process of the sample was covered by dense $FeCO_3$ crystals, the aggressive ions such as CO_3^{2-}, Cl^- can penetrate through the weak sites, reaching the steel substrate as shown in Fig. 8. In the presence of H^+, the fast dissolution occurs at Ca^{2+} co-precipitation sites and acts as pathways for the penetration of aggressive ions, which promotes the subsequent local corrosion processes and develops into pores/gaps on the surface. In both cases, the preferential dissolution occurs at the grain boundary or locally, indicating a high risk of potential to induce localised corrosion on the surface, resulting in a major threat to the pipeline integrity. The current study yields atomistic insights into the interactions and weak spots involved in complex corrosion products and can serve as the input data to guide the corrosion prediction of carbon steel used in geothermal production applications.

In summary, we compare the characteristics of the naturally formed corrosion product layer in CO_2-saturated formation water in the presence or absence of Ca^{2+} ions, and focus on the degradation mechanism for iron-calcium mixed carbonates layers and compared with pure iron carbonate scale in acidification conditions. The following main conclusions can be made:

1. The co-precipitation of Ca^{2+} into iron carbonate increases the bond length between cation and oxygen and expands the lattice volume.
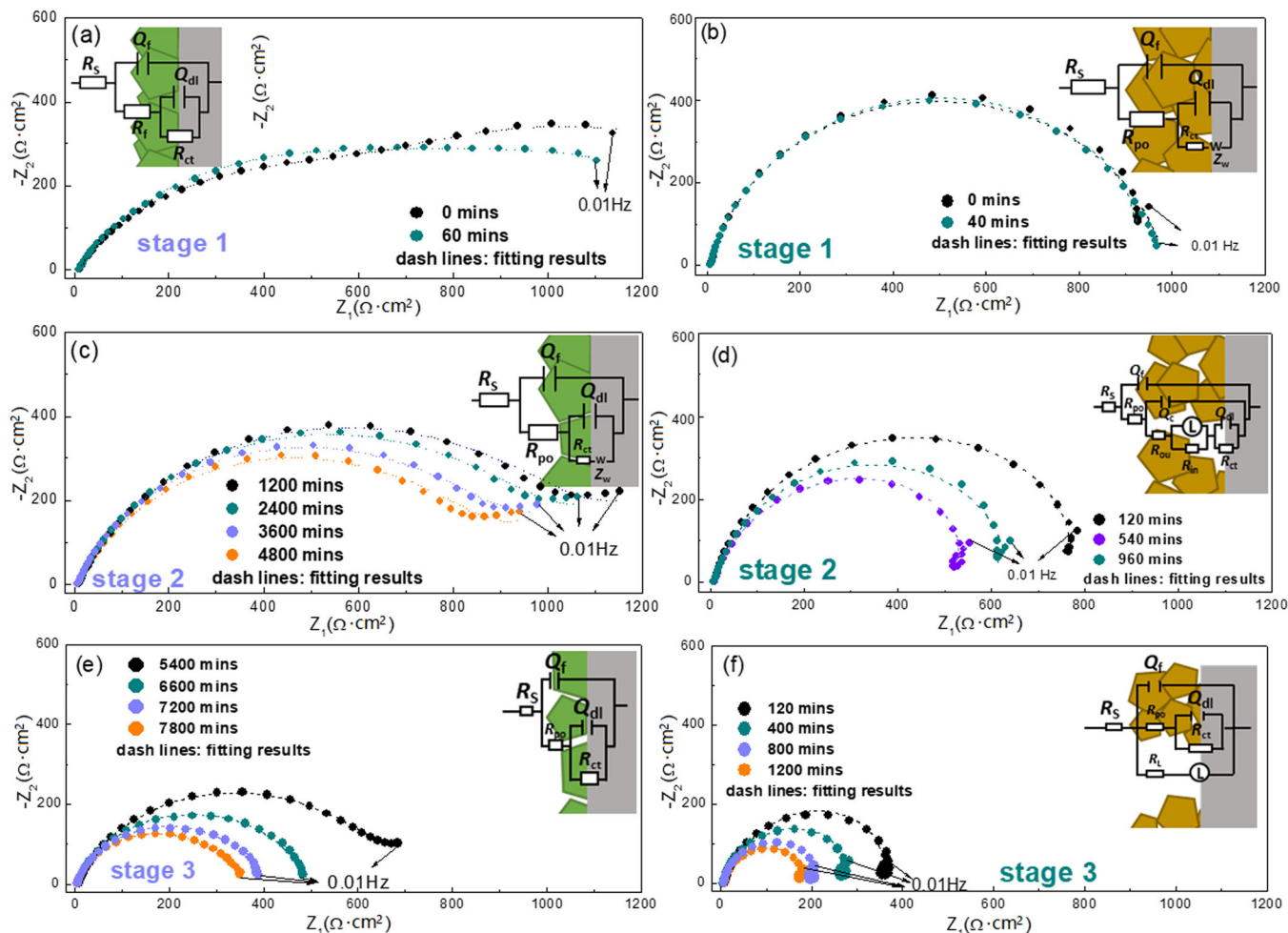
Fig. 7 Nyquist plots of the dissolution experiments. (a), (c) and (e) for carbon steel covered with $FeCO_3$, (b), (d) and (f) for carbon steel covered with $Ca_{0.51}Fe_{0.49}CO_3$ scales at various stages along with Fig. 6.

2. The Ca^{2+} co-precipitated position acts as weak sites and is favourable to breakdown, leading to local dissolution and accelerating the penetration rate of carbon steel.

3. Although both Fe–O and C–O bonds within $Ca_{1-x}Fe_xCO_3$ can be broken in a condition at a lower pH, $FeCO_3$ presents better stability than $Ca_{0.51}Fe_{0.49}CO_3$. The weak bonds between Ca^{2+} and CO_3^{2-} promote the preferential dissolution in Ca-containing region, leaving a porous corrosion product layer consist of a high proportion of Fe.

4. The experimental results indicated that the presence of Ca-rich areas was detected locally and mainly found in the pores after the dissolution experiments, suggesting that the growth of $Ca_{1-x}Fe_xCO_3$ scales contains ununiform Ca mole fraction and results in the preferential dissolution occurred locally on the surface.

METHODS

Preparation of naturally formed corrosion scales

Carbon steel specimens (API 5L X65) were cut from a bar (15-mm diameter, BAO steel) and the thickness is 6 mm. The elemental composition of carbon steel specimens consisted of 0.260 wt.% C, 0.32 wt.% Si, 0.43 wt.% Mn, 0.008 wt.% P, 0.005 wt.% S, 0.490 wt.% Cr, 0.8 wt.% Mo, 0.037 wt.% Ni, 0.080 wt.% V, ≤0.010 wt.% Ti, and balance with Fe. The specimens used for the electrochemical testing were sealed in resin to leave one surface with an exposure area of 1.77 cm^2 to the solution. All these specimens were ground the entire surface from 120 to 800 grit SiC papers, rinsed with

distilled water, acetone, and ethanol, then dried with compressed nitrogen gas. Prepared specimens were stored in a vacuum desiccator and used within 10 min. The in situ autoclave setup is provided in Supplementary Fig. 1. Three immersion specimens and three electrochemical specimens were placed within the autoclave separately for each test, generating a volume to surface ratio of 33 ml/cm^2. The autoclave sealed at ambient temperature and the whole system was flushed with high-pressure CO_2 to remove the remaining O_2, then pumping in the prepared solutions (solution 1: CO_2-saturated 3 wt.% NaCl, 0.08 wt.% $NaHCO_3$ solution; solution 2: CO_2-saturated 1.54 wt.% NaCl, 1.83 wt.% $CaCl_2 \cdot 2H_2O$, 0.08 wt.% $NaHCO_3$ solution, maintained Cl^- concentration constant and $O_2 < 10$ ppb), followed by pressurising the autoclave to 20 bar with CO_2, then heated to 60 °C and the test duration is 72 h of exposure test to generate pure $FeCO_3$ layer or a mixture of $Ca_{1-x}Fe_xCO_3$ layer on the sample surface.

The naturally formed corrosion products were observed by scanning electron microscope (SEM, Hitachi, Regulus 8100). All images were collected at an accelerating voltage of 15 kV and a working distance of ~15.3 mm. The total composition of naturally formed corrosion scales was collected using X-Ray Diffraction (XRD, Bruker D8 ADVANCE) over a range of $2\theta = 20-70°$ at a step size of 0.033° per second. The compositions of corrosion scales provided with a HORIBA EX-350 AZtecEnergy energy disperse spectroscopy (EDS) system using spot scanning and mapping.

Dissolution of the naturally formed corrosion scales

The prepared specimens covered by corrosion scales were exposed to a CO_2-saturated 3 wt.% NaCl solution at 15 °C and pH 3.75. During the dissolution process, LPR was employed for tracking the dissolution of the corrosion scales and performed from −10 to 10 mV vs OCP at a scanning rate of 0.167 mV/s by Gamry workstation in a conventional three-electrode
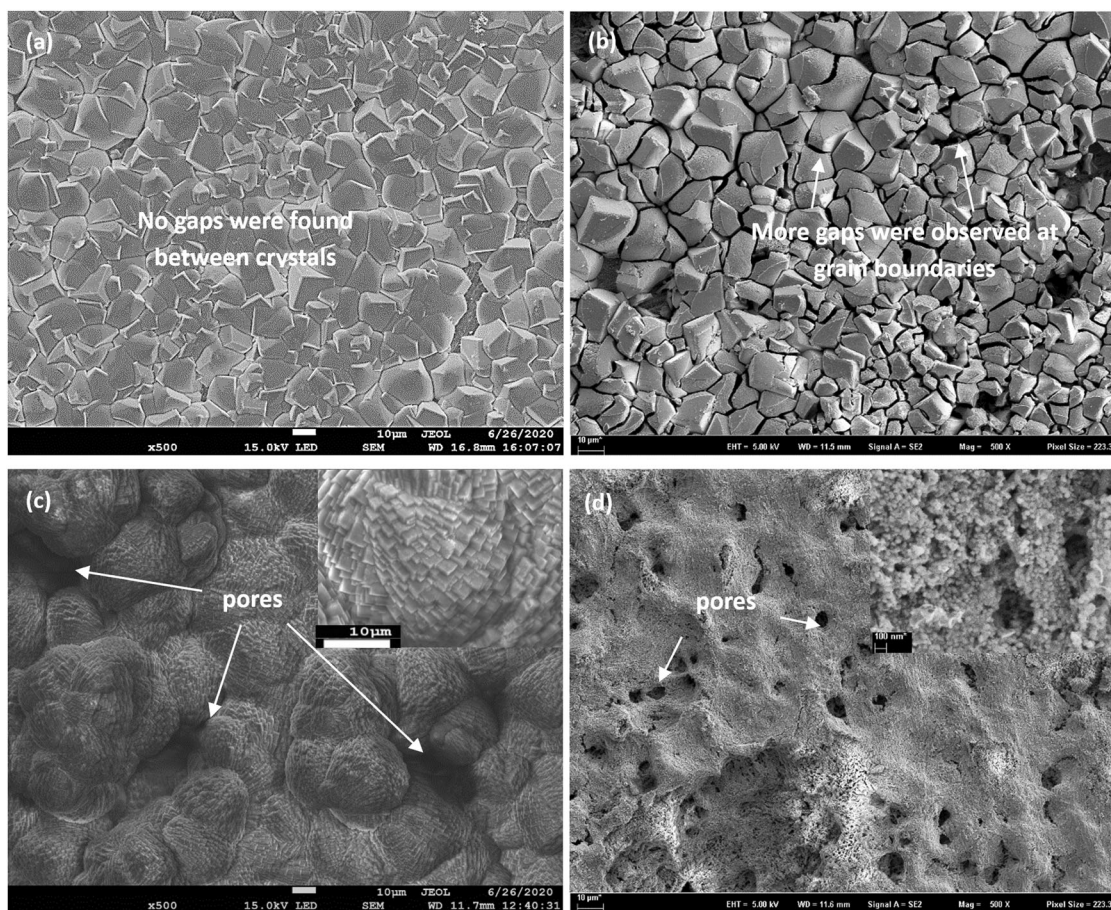
Fig. 8 The surface morphology of before/after dissolution experiment. a Crystalline $FeCO_3$ before dissolution experiment, **b** crystalline $FeCO_3$ after the dissolution experiment at 15 ℃; **c** Ca-containing corrosion scales before dissolution experiment, **d** Ca-containing corrosion scales after the dissolution experiment at 15 ℃.

cell. The prepared specimens were used as working electrode, platinum foil as the counter, and saturated calomel electrode (SCE) as a reference electrode, respectively. The EIS measurements at various dissolution stages were performed, which were monitored in the CO_2-saturated solution at OCP over a frequency range of 100 kHz to 10 mHz using 10 mV sinusoidal potential modulation. The electrochemistry data was analysed with surface morphology and corrosion product compositions at various dissolution stages via SEM, XRD, and EDS.

First-principle calculation

First-principles thermodynamics based on DFT were used to calculate the optimised atomistic and electronic structure of the naturally formed corrosion products. To simplify the model, typical corrosion products were selected, which are $FeCO_3$ (siderite), $Ca_{0.25}Fe_{0.75}CO_3$, $Ca_{0.5}Fe_{0.5}CO_3$, $Ca_{0.75}Fe_{0.25}CO_3$, and $CaCO_3$ (calcite) based on the experimental results via XRD, more details calculation of Ca and Fe mole fraction within the crystals can be found in our previous publications[21,22].

For siderite and calcite (inorganic crystal structure database, ICSD), supercells were constructed in (1 0 4) cleave surface. The $Ca_{0.25}Fe_{0.75}CO_3$, $Ca_{0.5}Fe_{0.5}CO_3$, and $Ca_{0.75}Fe_{0.25}CO_3$ supercells were constructed by replacing the Fe atoms in the interlayers with Ca atoms. Based on the geometry optimization model proposed by CASTEP, the generalized gradient approximation (GGA) exchange-correlation energy functional was used with the Perdew-Burke-Ernzerhof (PBE) method and the Kurdjumov-Sachs (KS) relationship. For the Fe-containing systems, a Hubbard U of 4.5 eV was employed for the correction of Fe 3d-electrons. The ultrasoft pseudopotential (USPP) was performed to describe the effective parameter of interaction between electrons and ion core, the cutoff energy is 380 eV for a plane-wave basis with a k-point set of 33334. The ionic relaxation was considered as convergence when the total energies below 10^{-5} eV and the force on every atom is less than 0.03 eV/Å.

DATA AVAILABILITY

The data that support the findings of this study are available from the corresponding author upon request.

REFERENCES

1. Ikeda, A., Mukai, S. & Ueda, M. Corrosion behavior of 9 to 25% Cr steels in wet CO2 environments. *Corrosion* **41**, 185–192 (1985).
2. Nesic, S., Postlethwaite, J. & Olsen, S. An electrochemical model for prediction of corrosion of mild steel in aqueous carbon dioxide solutions. *Corrosion* **52**, 280–294 (1996).
3. Springer, R. D., Wang, Z., Anderko, A., Wang, P. & Felmy, A. R. A thermodynamic model for predicting mineral reactivity in supercritical carbon dioxide: I. Phase behavior of carbon dioxide–water–chloride salt systems across the H_2O-rich to the CO_2-rich regions. *Chem. Geol.* **322**, 151–171 (2012).
4. Sun, W. & Nešic, S. Kinetics of corrosion layer formation: part 1—iron carbonate layers in carbon dioxide corrosion. *Corrosion* **64**, 334–346 (2008).
5. Zheng, L., Landon, J., Matin, N. S. & Liu, K. $FeCO_3$ coating process toward the corrosion protection of carbon steel in a postcombustion CO_2 capture system. *Ind. Eng. Chem. Res.* **55**, 3939–3948 (2016).
6. Hua, Y., Barker, R., Charpentier, T., Ward, M. & Neville, A. Relating iron carbonate morphology to corrosion characteristics for water-saturated supercritical CO_2 systems. *J. Supercrit. Fluids* **98**, 183–193 (2015).
7. Dugstad, A., Hemmer, H. & Seiersten, M. Effect of steel microstructure on corrosion rate and protective iron carbonate film formation. *Corrosion* **57**, 369–378 (2001).
8. Dugstad, A. Mechanism of Protective Film Formation During CO_2 Corrosion of Carbon Steel. in *NACE-98031* 11 (NACE International, 1998).

9. Crolet, J., Thevenot, N. & Nesic, S. Role of conductive corrosion products in the protectiveness of corrosion layers. *Corrosion* **54**, 194–203 (1998).

10. Hua, Y. et al. The formation of $FeCO_3$ and Fe_3O_4 on carbon steel and their protective capabilities against CO_2 corrosion at elevated temperature and pressure. *Corros. Sci.* **157**, 392–405 (2019).

11. Hua, Y., Barker, R. & Neville, A. Comparison of corrosion behaviour for X-65 carbon steel in supercritical CO_2-saturated water and water-saturated/unsaturated supercritical CO_2. *J. Supercrit. Fluids* **97**, 224–CO237 (2015).

12. Sk, M. H. et al. Local supersaturation and the growth of protective scales during CO_2 corrosion of steel: effect of pH and solution flow. *Corros. Sci.* **126**, 26–36 (2017).

13. Guo, S., Xu, L., Zhang, L., Chang, W. & Lu, M. Corrosion of alloy steels containing 2% chromium in CO_2 environments. *Corros. Sci.* **63**, 246–258 (2012).

14. Guo, S., Xu, L., Zhang, L., Chang, W. & Lu, M. Characterization of corrosion scale formed on 3Cr steel in CO_2-saturated formation water. *Corros. Sci.* **110**, 123–133 (2016).

15. Gao, M., Pang, X. & Gao, K. The growth mechanism of CO_2 corrosion product films. *Corros. Sci.* **53**, 557–568 (2011).

16. Ahmad, E. A. et al. Corrosion protection through naturally occurring films: new insights from iron carbonate. *ACS Appl. Mater. Interfaces* **11**, 33435–33441 (2019).

17. Tanupabrungsun, T., Brown, B., & Nesic, S. Effect of pH on CO_2 corrosion of mild steel at elevated temperatures in NACE-2348 1 (NACE International, 2013).

18. Han, J., Yang, Y., Brown, B. & Nesic, S. Electrochemical investigation of localized CO_2 corrosion on mild steel. in NACE-07323 (NACE International, 2007).

19. Tavares, L. M., da Costa, E. M., de Oliveira Andrade, J. J., Hubler, R. & Huet, B. Effect of calcium carbonate on low carbon steel corrosion behavior in saline CO_2 high pressure environments. *Appl. Surf. Sci.* **359**, 143–152 (2015).

20. Esmaeely, S. N., Young, D., Brown, B. & Nešić, S. Effect of incorporation of calcium into iron carbonate protective layers in CO_2 corrosion of mild steel. *Corrosion* **73**, 238–246 (2017).

21. Hua, Y., Shamsa, A., Barker, R. & Neville, A. Protectiveness, morphology and composition of corrosion products formed on carbon steel in the presence of Cl-, Ca^{2+} and $Mg2^+$ in high pressure CO_2 environments. *Appl. Surf. Sci.* **455**, 667–682 (2018).

22. Shamsa, A. et al. The role of Ca^{2+} ions on Ca/Fe carbonate products on X65 carbon steel in CO_2 corrosion environments at 80 and 150 °C. *Corros. Sci.* **156**, 58–70 (2019).

23. Powell, R., Condliffe, D. M. & Condliffe, E. Calcite–dolomite geothermometry in the system $CaCO_3$–$MgCO_3$–$FeCO_3$: an experimental study. *J. Metamorph. Geol.* **2**, 33–41 (1984).

24. Hossain, F. M., Murch, G. E., Belova, I. V. & Turner, B. D. Electronic, optical and bonding properties of $CaCO_3$ calcite. *Solid State Commun.* **149**, 1201–1203 (2009).

25. Brik, M. First-principles calculations of structural, electronic, optical and elastic properties of magnesite $MgCO_3$ and calcite $CaCO_3$. *Phys. B Condens. Matter* **406**, 1004–1012 (2011).

26. Escamilla-Roa, E., Sainz-Díaz, C. I., Huertas, F. J. & Hernandez-Laguna, A. Adsorption of molecules onto (1014) dolomite surface: an application of computational studies for microcalorimetry. *J. Phys. Chem. C* **117**, 17583–17590 (2013).

27. Golosova, N. et al. Magnetic and structural properties of $FeCO_3$ at high pressures. *Phys. Rev. B* **96**, 134405 (2017).

28. Hsu, H. & Huang, S.-C. Spin crossover and hyperfine interactions of iron in (Mg, Fe) CO_3 ferromagnesite. *Phys. Rev. B* **94**, 060404 (2016).

29. Shi, H., Luo, W., Johansson, B. & Ahuja, R. First-principles calculations of the electronic structure and pressure-induced magnetic transition in siderite $FeCO_3$. *Phys. Rev. B* **78**, 155119 (2008).

30. Yue, X. et al. Evolution and characterization of the film formed on super 13Cr stainless steel in CO_2-saturated formation water at high temperature. *Corros. Sci.* **163**, 108277 (2020).

31. Yue, X., Zhang, L., Sun, C., Xu, S., Wang, C., Lu, M., ... & Hua, Y. A thermodynamic and kinetic study of the formation and evolution of corrosion product scales on 13Cr stainless steel in a geothermal environment. *Corros. Sci.* **169**, 108640 (2020).

32. Yue, X. et al. Influence of a small velocity variation on the evolution of the corrosion products and corrosion behaviour of super 13Cr SS in a geothermal CO_2 containing environment. *Corros. Sci.* **178**, 108983 (2020).

33. Zhu, J., Xu, L. & Lu, M. Electrochemical impedance spectroscopy study of the corrosion of 3Cr pipeline steel in simulated CO_2-saturated oilfield formation waters. *Corrosion* **71**, 854–864 (2015).

34. Cao, C. N. & Zhang, J. Q. *An Introduction of Electrochemical Impedance Spectroscopy Science*. vol. 9.5 (Science Press, 2002).

ACKNOWLEDGEMENTS

AUTHOR CONTRIBUTIONS
X.Y. performed the density functional theory calculations and analyzed the results with the help of Y.H. and L.Z. X.Y. and Y.H. wrote the manuscript and performed the experiments. Data interpretation was discussed among all authors.

COMPETING INTERESTS
The authors declare no competing interests.

ADDITIONAL INFORMATION
Supplementary information The online version contains supplementary material available at https://doi.org/10.1038/s41529-021-00152-x.

Correspondence and requests for materials should be addressed to Y.H.

Reprints and permission information is available at http://www.nature.com/reprints

Publisher's note Springer Nature remains neutral with regard to jurisdictional claims in published maps and institutional affiliations.